

SpARCD: A Spectral Graph Framework for Revealing Differential Functional Connectivity in fMRI Data

Shira Yoffe^a, Ziv Ben-Zion^c, Talma Hendler^{d,e,f,g}, Malka Gorfine^b, Ariel Jaffe^a

^a*Department of Statistics and Data Science, Hebrew University of Jerusalem, Jerusalem, Israel*

^b*Department of Statistics and Operations Research, Tel Aviv University, Tel Aviv, Israel*

^c*School of Public Health, Faculty of Social Welfare and Health Sciences, University of Haifa, Haifa, Israel*

^d*Sagol School of Neuroscience, Tel Aviv University, Tel Aviv, Israel*

^e*Sagol Brain Institute, Tel Aviv Sourasky Medical Center, Tel Aviv, Israel*

^f*Gray Faculty of Medical and Health Sciences, Tel Aviv University, Tel Aviv, Israel*

^g*School of Psychological Sciences, Faculty of Social Sciences, Tel Aviv University, Tel Aviv, Israel*

Abstract

Identifying brain regions that exhibit altered functional connectivity across cognitive or emotional states is a key problem in neuroscience. Existing methods, such as edge-wise testing, seed-based psychophysiological interaction (PPI) analysis, or correlation network comparison, typically suffer from low statistical power, arbitrary thresholding, and limited ability to capture distributed or nonlinear dependence patterns. We propose SpARCD (Spectral Analysis of Revealing Connectivity Differences), a novel statistical framework for detecting differences in brain connectivity between two experimental conditions. SpARCD leverages distance correlation, a dependence measure sensitive to both linear and nonlinear associations, to construct a weighted graph for each condition. It then constructs a differential operator via spectral filtering and uncovers connectivity changes by computing its leading eigenvectors. Inference is achieved via a permutation-based testing scheme that yields interpretable, region-level significance maps. Extensive simulation studies demonstrate that SpARCD achieves superior power relative to conventional edge-wise or univariate approaches, particularly in the presence of complex dependency structures. Application to fMRI data from 113 early PTSD patients performing an emotional face-matching task reveals dis-

tinct networks associated with emotional reactivity and regulatory processes. Overall, SpARCD provides a statistically rigorous and computationally efficient framework for comparing high-dimensional connectivity structures, with broad applicability to neuroimaging and other network-based scientific domains.

Keywords: Graph theory, Neuroimaging, Distance correlation, fMRI scans, PTSD,

1. Introduction

Identifying variables associated with distinct biological or clinical states is a crucial task across many scientific disciplines (Smyth, 2004; Love et al., 2014). In many applications, differences between states do not arise from the additive effects of a small number of independent variables, but rather from coordinated changes in groups of interdependent variables (Daudt et al., 2018; Xiao et al., 2018; Zhao et al., 2021). In genetics, for example, pathway-based analyses aggregate signals from related genetic variants to capture coordinated effects (Wang et al., 2010). Similarly, in neuroimaging, coordinated activity within brain networks has been linked to behavior and clinical outcomes (Smith et al., 2009; Crossley et al., 2013). Motivated by this principle, we develop a framework for uncovering brain networks from functional magnetic resonance imaging (fMRI) scans.

fMRI is a non-invasive neuroimaging technique that measures brain activity indirectly through blood-oxygen-level-dependent (BOLD) signals, reflecting changes in local blood oxygenation that are tightly coupled to neural activity (Logothetis, 2008). One of the primary challenges of fMRI analysis is that the activation level, measured through BOLD signals, can differ substantially between individuals, irrespective of their clinical states. To overcome this limitation, researchers often turn to functional connectivity (FC), a widely used measure for large-scale brain organization. FC is typically estimated by analyzing the statistical dependencies between BOLD time series recorded from different spatial regions of the brain. FC captures coordinated activity that is often more stable and reproducible than region-wise activation levels, and has been successfully used to predict cognitive traits and clinical status (Mohanty et al., 2020; Finn et al., 2015; Van Dijk et al., 2010). The robustness of FC has made it a central tool for studying brain networks associated with cognitive, emotional, and clinical differences

(Greicius et al., 2004; Anand et al., 2005; Liao et al., 2010). However, reliably detecting connectivity changes remains challenging due to the high dimensionality and complex interdependencies among brain regions (Zalesky et al., 2010).

To uncover changes in FC between states, traditional approaches test the connectivity between each pair of regions independently. This approach results in a number of tests that scales quadratically with the number of regions, significantly reducing statistical power. Alternative methods focus on connectivity between a single region of interest (ROI) and all other regions (Friston et al., 1997; McLaren et al., 2012). While these methods reduce the number of tests, they may overlook distributed network changes essential for understanding clinical phenomena (Gerchen et al., 2014; Li et al., 2023). These limitations motivate the development of novel methods for detecting network-level differences between conditions.

In this work, we introduce *SpARCD* (Spectral Analysis for Revealing Connectivity Differences), a novel approach for detecting brain networks inspired by recent advances in spectral graph theory. For each condition, our method constructs a graph whose nodes represent brain regions and whose edges encode their functional connectivity. The problem of identifying brain networks that distinguish two conditions can thus be formulated as a graph-theoretic task: given two graphs with identical node sets but differing edge weights, detect subsets of nodes whose connectivity profiles differ significantly between the graphs. This spectral formulation provides an efficient, interpretable framework for uncovering network alterations.

Our primary motivating application for SpARCD is the analysis of fMRI data collected under the Emotional Face Matching Task (EFMT, or Hariri task) (Hariri et al., 2002). The Hariri protocol is a widely used framework for probing emotional reactivity and identifying neural changes associated with emotional processing (Savage et al., 2024). During the task, participants match faces displaying various emotional expressions and geometric shapes that serve as controls, yielding BOLD signals corresponding to emotional and neutral conditions. This design allows for within-subject comparisons of emotional and neutral states. Prior studies of EFMT revealed FC alterations in conditions such as alcohol use disorder (Gorka et al., 2013; O'daly et al., 2012), depression (Carballido et al., 2011), and schizophrenia (Goghari et al., 2017). Here, we analyze fMRI scans of PTSD participants, where previous work has extensively examined activation patterns in emotion-related brain regions. Investigating dysregulated connectivity patterns among these

regions can provide unique insights into the neural basis of PTSD and reveal mechanisms underlying symptom development (Shin and Liberzon, 2010; Etkin and Wager, 2007; Sripada et al., 2012).

1.1. Problem Setting

In this work, we analyzed fMRI data from the cohort described in Ben-Zion et al. (2019). The study enrolled 171 adults who underwent clinical and neuroimaging assessments at three post-trauma time points: one month, six months, and fourteen months. Sixteen participants were excluded due to incomplete or poor-quality imaging at the first session, yielding a final cohort of 155 individuals, of whom 113 met full PTSD criteria at the first time-point. Our analysis focuses on resting-state fMRI and the EFMT taken at the first time point, one month post-trauma. This cohort is notable for its large sample size relative to typical neuroimaging studies, the early timing of scanning (one month after trauma), and the deliberate inclusion of participants with high PTSD symptom severity. These features provide a unique opportunity to investigate neural correlates of emotion processing and early markers of PTSD shortly after trauma exposure.

The EFMT followed the Hariri protocol (Hariri et al., 2002), where each participant underwent an fMRI session that consisted of alternating blocks with emotional and neutral visual stimuli. The emotional blocks included images of faces displaying anger, fear, surprise, or neutrality, while the neutral blocks featured geometric shapes, specifically circles and ovals. Participants were instructed to match each image to a target as quickly and accurately as possible. The task consisted of four blocks of facial expressions and five blocks of shapes. For our analysis, we excluded the first block of shapes, corresponding to the initial scanning block, due to its higher noise levels.

The data analysis presented in this work is based on a parcellation of the fMRI scans into $R = 113$ ROIs defined by the Harvard–Oxford atlas, comprising 96 bilateral cortical regions and 17 subcortical regions.

Parcellating the fMRI recordings from the two conditions yields two corresponding datasets: $X \in \mathbb{R}^{n_x \times R \times T}$, $Y \in \mathbb{R}^{n_y \times R \times T}$, where R denotes the number of ROIs, T the number of time samples, and n_x, n_y are the number of scans in condition X and Y , respectively. The datasets X and Y may be paired, such that every scan in X corresponds to a scan in Y , or may be unpaired. Our goal is to identify brain networks whose FC patterns differ between the two conditions. To facilitate clarity in the upcoming technical sections, we summarize key notation used throughout the paper in Table 1.

1.2. Related Work

Many studies have analyzed functional connectivity (FC) between brain regions to gain insight into the organization of brain networks (Van Den Heuvel and Pol, 2010). A common strategy is to test each edge separately, for example, by comparing correlation coefficients between groups and correcting for multiple comparisons (Whitfield-Gabrieli and Nieto-Castanon, 2012). Such procedures, typically based on controlling the False Discovery Rate (FDR), substantially reduce statistical power and may miss effects with weak neuronal signal (Nichols and Hayasaka, 2003; Eklund et al., 2016; Zhang et al., 2011). Moreover, univariate tests are inherently limited in their ability to capture coordinated, subnetwork-level alterations (Zalesky et al., 2010).

The Network-Based Statistic (NBS) (Zalesky et al., 2010) is a statistical framework designed to address the multiple-comparison problem in edge-wise connectivity analyses by computing a graph whose nodes and edge weights represent brain regions and some measure of statistical association between them. The method computes a sparse graph by applying a threshold to the graph's connectivity matrix and identifies connected components (subnetworks) within the sparse graph. Finally, a subnetwork-level statistic, such as the subnetwork's size or summed edge weights, is computed and assessed for significance via permutation testing. By aggregating effects across interconnected edges, NBS increases sensitivity to distributed network-level changes, though its dependence on a fixed primary threshold may reduce robustness and limit detection of small or overlapping effects.

Psychophysiological interaction (PPI) analysis is another widely used approach (Friston et al., 1997) that has been shown to produce robust and reproducible results (Smith et al., 2016). In contrast to network-level approaches, PPI estimates how task-related changes in neuronal activity modulate the connectivity between a seed region and the rest of the brain. However, its main limitation is its reliance on a single a priori seed selection, which can affect the reliability of the results (Li et al., 2023). In addition, PPI may provide a partial view of FC, since it does not take into account interactions between non-seed regions (Gerchen et al., 2014).

In this work, we introduce a graph-based method for detecting changes in functional connectivity between two fMRI states, which is based on differences in the leading eigenvectors between graphs. Graph-based methodologies were proposed for various tasks in fMRI analysis. For example, small-world network measures have been used to characterize alterations in conditions such as Alzheimer's disease (Sanz-Arigita et al., 2010). Within

this framework, geodesic-distance-based metrics such as characteristic path length and global efficiency quantify network-level communication and integration. These measures have been shown to be sensitive to disease-related changes in FC (Bullmore and Sporns, 2009; Liao et al., 2010). Jacob et al. (2016, 2019) derived DepNA, which models directed influence relationships among regions, and used it to examine whether connectivity hierarchies distinguish patients with social anxiety disorder from controls. The work of Ben Simon et al. (2017) evaluates the relative contribution of each ROI to the separation between two psychological states. Spectral graph-based approaches have also been applied to fMRI data to uncover functional organization. For instance, spectral clustering has been utilized to create functionally homogeneous parcellations from resting-state fMRI data (Craddock et al., 2012; Shen et al., 2013). Additionally, Cribben and Yu (2017) applied spectral methods to detect changes in network structure. Cahill et al. (2016) utilized spectral methods for group-wise functional community detection.

Here, we focus on spectral graph analysis, which examines the eigenstructure of graph Laplacians to reveal differences in connectivity patterns between states (Sristi et al., 2022; Yoffe et al., 2024). Our contributions are threefold: (i) Network-level characterization. We develop an approach specifically designed to capture coordinated shifts in network structure. For each dataset corresponding to a specific state (e.g., a particular stimulus condition), we construct a graph whose edge weights represent estimates of FC between pairs of regions. We estimate FC using distance correlation (Székely et al., 2007), which captures both linear and nonlinear dependencies. Instead of exhaustive pairwise comparisons, we identify meaningful differences in network organization by comparing the leading eigenvectors of the respective Laplacians. (ii) Statistical inference. We propose a permutation-based framework for assessing the statistical significance of these spectral differences, explicitly accounting for data dependencies and yielding interpretable region-level significance scores. (iii) Empirical validation. Through extensive simulations and an application to fMRI data from PTSD patients engaged in an emotional reactivity task, we demonstrate the utility of the proposed method in uncovering clinically relevant, network-level alterations distinguishing emotional from neutral states.

Symbol	Dimensions	Description
X	$\mathbb{R}^{n \times R \times T}$	Tensor containing the signal matrices of R brain regions for n samples across T time points (similarly for Y).
$X^{(i)}$	$\mathbb{R}^{R \times T}$	Signal matrix of the i -th sample (similarly $Y^{(i)}$).
X_r	$\mathbb{R}^{n \times T}$	Signal matrix of the r -th region across n samples (similarly Y_r).
L_X	$\mathbb{R}^{R \times R}$	Symmetric normalized Laplacian matrix computed on X (similarly L_Y).
$v_X^{(k)}$	\mathbb{R}^R	k -th eigenvector of L_X (similarly $v_Y^{(k)}$).
Q_X	$\mathbb{R}^{R \times R}$	Projection matrix onto the subspace orthogonal to the leading K eigenvectors of L_X (similarly Q_Y).
\tilde{L}_X	$\mathbb{R}^{R \times R}$	Differential operator for L_X (similarly \tilde{L}_Y).
$s(r)$	\mathbb{R}	Test statistic for region r .
Σ_X	$\mathbb{R}^{R \times R}$	Block-diagonal covariance matrix (similarly Σ_Y).
$S_X^{(i)}$	$\mathbb{R}^{q \times T}$	Set of q seed signals for $X^{(i)}$ (similarly $S_Y^{(i)}$).
$s_{\text{PPI}}(r)$	\mathbb{R}	Summary measure for the r -th region obtained from the PPI-based method.
$s_{\text{UC}}(r, r')$	\mathbb{R}	Summary measure for the r -th region obtained from the UC method.

Table 1: Summary of Notation

2. Relevant Background

Our method for identifying networks that differentiate between two states is based on constructing a separate graph for each state using the corresponding fMRI scans. In this section, we briefly review two topics relevant to our approach. Section 2.1 introduces key definitions required to understand the spectral analysis of the dual graphs. In our framework, the weight between two nodes represents the estimated FC between the corresponding brain regions. Unlike previous studies, we estimate FC using distance correlation (Székely et al., 2007). Section 2.2 formally defines distance correlation and explains why it is particularly well-suited for quantifying FC between brain regions.

2.1. Spectral Graph Analysis

Functional connectivity, as estimated from fMRI, can be effectively modeled using a graph framework. In this representation, each node corresponds to a distinct brain region, and the weight of an edge between two nodes reflects their FC. Specifically, let G_X and G_Y denote two undirected and weighted graphs, each comprising R nodes, corresponding to distinct brain regions. The pairwise statistical association between regions, typically derived from measures such as correlation, is encoded in the symmetric weight matrices $W_X, W_Y \in \mathbb{R}^{R \times R}$.

For each graph, we define a corresponding *degree matrix*, $C_X, C_Y \in \mathbb{R}^{R \times R}$, which are diagonal matrices containing the total connectivity (degree) of each node. Specifically,

$$C_X(r, r) = \sum_{r'=1}^R W_X(r, r') , \quad C_Y(r, r) = \sum_{r'=1}^R W_Y(r, r') .$$

Thus, $C_X(r, r)$ represents the overall strength of connections for node r in graph X ; that is, it is the sum of all edge weights linking node r to the other regions. In the context of brain networks, $C_X(r, r)$ can be interpreted as the total functional connectivity of brain region r with the rest of the brain under condition X .

We construct the *symmetric normalized Laplacian matrices*, L_X and L_Y , by

$$L_X = I_R - C_X^{-1/2} W_X C_X^{-1/2} , \quad L_Y = I_R - C_Y^{-1/2} W_Y C_Y^{-1/2} , \quad (1)$$

where $I_R \in \mathbb{R}^{R \times R}$ denotes the identity matrix. The normalized Laplacian matrix encodes the structural properties of the graph in a manner that is particularly suitable for spectral analysis (Chung, 1997). Intuitively, each diagonal matrix C_X (or C_Y) reflects the total connectivity of a node, while L_X (or L_Y) balances this connectivity against the weights of its edges. This emphasizes relative connectivity patterns rather than raw connection strength, thereby highlighting global and local structural features of the network. In the context of brain networks, the normalized Laplacian captures how strongly each brain region is connected relative to its overall connectivity profile, allowing us to characterize condition-specific differences in brain organization.

The eigenvectors of the graph Laplacian, denoted by $v_X^{(1)}, \dots, v_X^{(R)}$ and $v_Y^{(1)}, \dots, v_Y^{(R)}$, are ordered according to their corresponding eigenvalues. These eigenvectors are particularly informative as they capture fundamental modes

of variation within the network (Von Luxburg, 2007). In particular, the first $K \leq R$ eigenvectors (associated with the smallest eigenvalues) provide a low-dimensional embedding of the graph that preserves its global connectivity structure (Belkin and Niyogi, 2003; Coifman and Lafon, 2006). Such spectral representations have been widely applied in clustering (Ng et al., 2001), manifold learning (Belkin and Niyogi, 2003; Coifman and Lafon, 2006), and network comparison (Wilson and Zhu, 2008). In our context, the spectral embeddings provide a structured feature representation for each brain region, enabling compact but yet, informative comparisons of connectivity patterns across conditions.

2.2. Distance Correlation

Distance correlation is a measure of dependency between two paired sets of vectors with potentially different dimensionalities (Székely et al., 2007). In our setting, we use distance correlation to estimate FC between two brain regions. Let the BOLD activity in regions r and r' across n subjects be represented by matrices $X_r \in \mathbb{R}^{n \times T}$ and $X_{r'} \in \mathbb{R}^{n \times T}$, respectively. To estimate the distance correlation (dCor), we first compute the pairwise Euclidean distance matrices D_r and $D_{r'}$, both of dimension $n \times n$. Denote by $\mathbf{1}_n$ a vector of ones of size n , by I_n an identity matrix of size $n \times n$, and by $H = I_n - \mathbf{1}_n \mathbf{1}_n^T / n$ the centering operator that projects a vector onto the complement subspace of $\mathbf{1}_n$. The centered distance matrices are then given by $\tilde{D}_r = HD_rH$ and $\tilde{D}_{r'} = HD_{r'}H$, which ensures that their row and column sums are zero. For two matrices A and B , let the inner product be defined as $\langle A, B \rangle = \sum_{ij} A_{ij} B_{ij}$. The estimator of the distance correlation measure between X_r and $X_{r'}$ is then

$$\mathcal{D}(X_r, X_{r'}) = \frac{\langle \tilde{D}_r, \tilde{D}_{r'} \rangle}{\sqrt{\langle \tilde{D}_r, \tilde{D}_r \rangle \langle \tilde{D}_{r'}, \tilde{D}_{r'} \rangle}}. \quad (2)$$

The distance correlation possesses several properties that make it particularly suitable for estimating FC between brain regions. The value of $\mathcal{D}(X_r, X_{r'})$ is bounded between 0 and 1, and equals zero only if X_r and $X_{r'}$ are statistically independent. Since it is based on Euclidean distances, distance correlation is invariant to rotations, scaling, and translations of X_r and $X_{r'}$. Most importantly, it captures nonlinear dependencies between X_r and $X_{r'}$, which linear correlation measures fail to detect. One limitation of applying distance correlation is its computational cost, which scales as $\mathcal{O}(n^2)$ due to the computation of D_r and $D_{r'}$.

3. SpARCD: Spectral Analysis for Revealing Connectivity Differences

We propose a method for identifying brain regions whose connectivity patterns differ between two states or conditions (e.g., faces versus shapes). The approach represents the functional connectivity structure of each state as a graph, where nodes correspond to brain regions, and edges reflect statistical associations between them. To compare the two conditions, we employ a spectral graph-based framework that captures differences in the global organization of the networks. These differences are then projected back onto individual brain regions, producing a quantitative score that reflects the degree to which each region's connectivity profile varies between conditions.

The algorithm steps are presented using a flowchart in Figure 1 and can be described in a four-step procedure: (I) compute two connectivity graphs that represent the average connectivity among regions in each state; (II) apply a spectral differential operator to these connectivity graphs in order to highlight structural differences between the two conditions; (III) compute a test statistic for each brain region, reflecting the extent to which its connectivity pattern differs between conditions; and (IV) perform a permutation test to assess the statistical significance of these regional differences. We next describe each of these steps in detail.

Step I: For each pair of regions (r, r') , we compute the sample distance correlation between their respective signal matrices and use it as the edge weight connecting them. This yields two symmetric weight matrices

$$W_X(r, r') = \mathcal{D}(X_r, X_{r'}) , \quad W_Y(r, r') = \mathcal{D}(Y_r, Y_{r'}) , \quad (3)$$

corresponding to the two conditions under comparison, where $\mathcal{D}(\cdot, \cdot)$ denotes the sample distance correlation, as described earlier. These matrices define the pairwise association structure for each state. We then compute the corresponding graph Laplacians L_X and L_Y using Eq. (1), which serve as our representations of functional connectivity in each state.

Step II: Let Q_X and Q_Y denote the projection matrices onto the subspaces orthogonal to the leading K eigenvectors of L_X and L_Y , respectively,

$$Q_X = I_R - \sum_{k=1}^K v_X^{(k)} v_X^{(k)T} , \quad Q_Y = I_R - \sum_{k=1}^K v_Y^{(k)} v_Y^{(k)T} . \quad (4)$$

The parameter K controls the number of meaningful eigenvectors retained from each graph. In the supplementary materials, we provide a simple

data-driven method for setting the value of K . The leading eigenvectors of a graph Laplacian span the subspace corresponding to its most dominant (low-frequency) connectivity patterns (Chung, 1997). Therefore, structural similarities between the graphs L_X and L_Y will tend to be captured within these top eigenvectors. To isolate differences, we construct filtered operators by projecting each graph onto the orthogonal complement of the other graph's dominant subspace

$$\tilde{L}_Y = Q_X(I_R - L_Y)Q_X, \quad \tilde{L}_X = Q_Y(I_R - L_X)Q_Y.$$

This projection removes components of L_Y (or L_X) that lie in the direction of the leading connectivity patterns of L_X (or L_Y), effectively filtering out shared structure and emphasizing differential connectivity.

Step III: To quantify the difference in connectivity between two graphs, we compute the difference between their respective differential operators via

$$L_d = \tilde{L}_Y - \tilde{L}_X.$$

The leading eigenvector of L_d , denoted by v_d , highlights the directions along which the operators differ the most, effectively capturing changes in connectivity between the two graphs. Entries of v_d with large positive or negative values indicate regions with substantial differences in connectivity. We define the test statistic for a region r by

$$s(r) = \frac{|v_d(r)|}{\|v_d\|_1},$$

where $\|\cdot\|_1$ is the L_1 norm. Note that the eigenvector v_d is L_2 normalized such that $\|v_d\|_2 = 1$. This ensures comparability across eigenvectors and allows the L_1 normalization in $s(r)$ to produce interpretable, unit-sum scores. $s(r)$ represents the relative importance of brain region r .

To illustrate the effect of ℓ_1 -normalization, we will examine two cases of vectors $x \in \mathbb{R}^n$ with $\|x\|_2 = 1$. First, consider a vector x , that has k dominant coordinates of order $1/\sqrt{k}$ and the remaining $n - k$ coordinates of order ε , where $0 < \varepsilon \ll 1/\sqrt{k}$. The ℓ_1 norm satisfies $\|x\|_1 \approx \sqrt{k} + (n - k)\varepsilon$. After ℓ_1 -normalization, the dominant entries scale as $\frac{1/\sqrt{k}}{\|x\|_1} \approx \frac{1/\sqrt{k}}{\sqrt{k} + (n - k)\varepsilon} \sim \frac{1}{k}$, while the small entries scale as $\varepsilon/(\sqrt{k} + (n - k)\varepsilon) \sim 0$, indicating that ℓ_1 -normalization amplifies sparsity. In contrast, for a balanced vector with all coordinates of order $1/\sqrt{n}$, we have $\|x\|_1 = \sqrt{n}$ and, after normalization,

all entries equal $1/n$, preserving balance. Thus, when $k \ll n$, the difference between these two cases becomes substantial. As a result, the normalization process highlights the distinction between balanced and imbalanced vectors, which is crucial for the permutation test discussed next.

Step IV:

The null hypothesis states that the BOLD signals have the same distribution under both conditions. Consequently, the Laplacians, representing group-level connectivity, under each condition are drawn from the same distribution. The alternative hypothesis states that the BOLD signals have different distributions across conditions.

To test these hypotheses, we employ a nonparametric permutation procedure. For each observation i , we randomly reassign condition labels to generate permuted datasets $\{\tilde{X}, \tilde{Y}\}$. Then, for each permutation b , we compute a test statistic $\tilde{s}^{(b)}$ from the permuted datasets. When the filtering parameter K in Eq. (4) is selected in a data-driven manner, it is re-estimated within each permutation to preserve the validity of the inference.

Under the null, any observed differences in connectivity arise solely from random variation, and the group-level test statistic satisfies,

$$s(r) \stackrel{d}{=} \tilde{s}^{(b)}(r) \quad ; \quad \forall r \in \{1, \dots, R\} \quad ; \quad \forall b \in \{1, \dots, B\}.$$

The empirical p -value for each region is computed as,

$$p_r = \frac{1}{B} \sum_{b=1}^B \mathbb{I}(\tilde{s}^{(b)}(r) \geq s(r)).$$

Since we test for R regions, we correct for multiple testing using the Benjamini–Hochberg procedure at a false discovery rate of $\alpha = 0.05$.

Block-level permutation for the Hariri protocol. In the Hariri protocol, each participant completes alternating blocks of emotional (face) and neutral (shape) stimuli. Within each block, the BOLD time series exhibits strong temporal dependence and reflects a sustained cognitive state induced by the stimulus. Consequently, individual time points are not exchangeable, and permutation at the time-point level would violate the exchangeability assumptions required for valid permutation inference. Instead, we treat each block as the basic unit of analysis. Under the null hypothesis that emotional and neutral conditions induce identical brain connectivity patterns, the distributions of

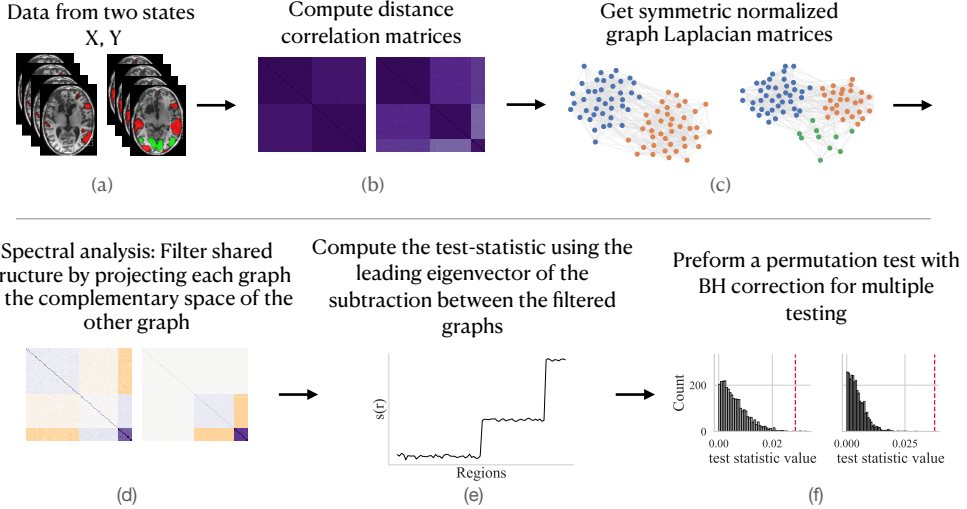


Figure 1: Flowchart describing the steps in the SpARCD algorithm.

blocks do not depend on the stimulus type. Therefore, block labels are exchangeable within each participant. This justifies a block-level permutation scheme, in which the observed blocks are randomly reassigned to the two conditions independently for each participant. This approach preserves the temporal coherence within blocks while respecting the experimental design and ensuring valid nonparametric inference.

4. Simulation Study

In this section, we evaluate the ability of our approach to identify brain regions whose connectivity patterns differ between two states. We assess its performance using artificial datasets designed to mimic common challenges encountered in fMRI analysis.

Across all experiments, we compare our method against two widely used approaches in the fMRI literature: (i) Psychophysiological Interaction (PPI), in which a summary measure for each region is computed based on its relation to a predefined seed region (Friston et al., 1997). We denote the summary measure for the r -th region by $s_{PPI}(r)$. (ii) Univariate correlation (UC) testing, which evaluates differences in pairwise correlations between conditions across all pairs of regions (Whitfield-Gabrieli and Nieto-Castanon, 2012). We

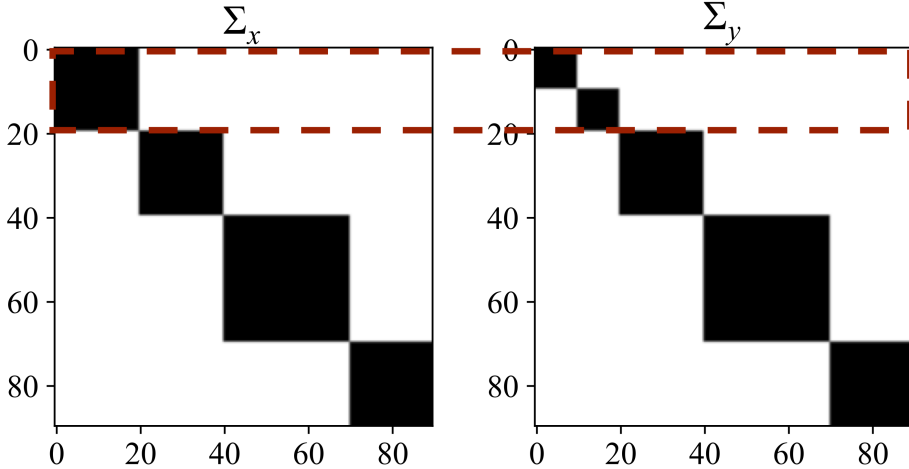


Figure 2: An example for the blow-dependency structure in states X and Y . One block in X is divided into two blocks in Y .

denote by $s_{UC}(r, r')$ the estimated mean Pearson correlation between regions r, r' . Additional implementation details for the PPI and UC methods are provided in the supplementary materials.

4.1. Data Generation

We considered a sample size of $n = 150$, a signal length of $T = 100$, and three types of connectivity profiles: (i) linear dependency structure, (ii) nonlinear dependency structure, and (iii) hybrid structures combining both linear and nonlinear components. In each experiment, we generated two sets of artificial signals, one for each state, with a block-dependency structure such that signals from two regions r and r' are dependent if they belong to the same block and independent otherwise. Let $l_X = \{l_X^{(1)}, \dots, l_X^{(q)}\}$ denote the sizes of the q dependency blocks in X . The block-dependency structures are identical across the two states, except for one block in state X , which is subdivided into two smaller blocks in state Y (see Fig. 2). The objective of each experiment is to correctly identify the regions comprising this modified block.

We generate data samples under linear dependency, which we denote $X_{(lin)}^{(i)}$, non-linear dependencies, denoted $X_{(nonlin)}^{(i)}$, and hybrid dependency. We describe each separately.

Linear setting. Each column of $X_{(lin)}^{(i)}$ was independently sampled from a multivariate Gaussian distribution with zero mean and a block-diagonal covariance matrix $\Sigma_X \in \mathbb{R}^{R \times R}$. Let $\Sigma_X^j \in \mathbb{R}^{l_X^{(j)} \times l_X^{(j)}}$ be the submatrix of Σ_X corresponding to the j -th block. Each block covariance is constructed as $\Sigma_X^j = U^j \Delta^j (U^j)^\top$, where U^j is a randomly drawn orthogonal matrix and Δ^j is a diagonal matrix with entries

$$\Delta^j(k, k) = \left(\frac{1}{k}\right)^\gamma, \quad k = 1, \dots, l^{(j)}.$$

The parameter γ controls the spectral decay within each block and thus determines the level of intra-block correlation. For example, setting $\gamma = 0$ yields the identity matrix, which corresponds to uncorrelated elements.

Parameters for linear setting. To increase the problem difficulty, we introduce heterogeneity across samples, such that for each sample, the block size vector ℓ_X was sampled from one out of the following three configurations,

$$\{20, 20, 30, 20\}, \quad \{20, 21, 29, 20\}, \quad \{20, 19, 31, 20\}$$

In Y , the first block was partitioned into two identical blocks. The partition was selected from one of the three following configurations

$$\{10, 10\}, \{9, 11\}, \{11, 9\}.$$

Nonlinear setting. We first generated, for each sample i , a set of d independent seed signals of length T , denoted $S_x^{(i)} \in \mathbb{R}^{d \times T}$. Each seed signal was drawn from a standard multivariate normal distribution

$$S_x^{(i)}(k, t) \sim \mathcal{N}(0, 1), \quad \text{for } k = 1, \dots, q \quad \text{and } t = 1, \dots, T. \quad (5)$$

For X , we used a fixed block size, denoted l . The seed signals were then embedded as the first feature in each block via

$$X_{(\text{nonlin})}^{(i)}(1 + B(k-1), t) = S_x^{(i)}(k, t) \quad k = 1, \dots, d.$$

The remaining features within each block ($r = 1, \dots, l-1$) were generated as nonlinear transformation of the corresponding seed signal using sine functions with random phases ϕ_r and frequencies f_r such that,

$$X_{(\text{nonlin})}^{(i)}(1 + l(k-1) + r, t) = \sin(\pi f_r S_x^{(i)}(k, t) + \phi_r) + \epsilon, \quad r = 1, \dots, (l-1), \quad k = 1, \dots, q$$

where $\epsilon \sim \mathcal{N}(0, \sigma^2 I)$ and σ^2 controls the noise level. As in the linear setting, the samples $Y_{(\text{nonlin})}^{(i)}$ were generated similarly to $X_{(\text{nonlin})}^{(i)}$, with a different block structure such that the last block in X is partitioned into two blocks in Y .

Parameters for nonlinear setting. The number of blocks in X and Y is set to $q = 8$ and $q + 1 = 9$, respectively, with $l = 18$ dependent features within each block.

Hybrid setting. We generated signals that combine the linear and non-linear dependency structure of the form

$$X^{(i)} = \alpha X_{(\text{lin})}^{(i)} + (1 - \alpha) X_{(\text{nonlin})}^{(i)} + \epsilon,$$

where $\epsilon \sim \mathcal{N}(0, \sigma^2 I)$, and $\alpha \in [0, 1]$ controls the relative contribution of the linear and non-linear components. The matrices $X_{(\text{lin})}^{(i)}$ and $X_{(\text{nonlin})}^{(i)}$ are generated as described above.

Parameters for hybrid setting. The number of blocks in X and Y is set to $q = 8$ and $q + 1 = 9$, respectively. The parameter γ that determines the level of dependency in the linear setting is set to 1.5.

4.2. Evaluation Metrics

We evaluate detection performance using three standard metrics: *precision*, *recall*, and the *area under the precision–recall curve (PR-AUC)*. These metrics quantify how accurately each method identifies truly differentiating brain regions, both when using continuous scores and at a fixed level of statistical significance.

Precision is defined as the proportion of detected regions that are truly differentiating,

$$\text{Precision} = \frac{\text{true positives}}{\text{number of detections}}.$$

Recall measures the proportion of truly differentiating regions that are successfully detected,

$$\text{Recall} = \frac{\text{true positives}}{\text{number of ground truth regions}}.$$

For each method, we compute a permutation-based p-value for every region and adjust for multiple comparisons using the BH procedure. Regions with BH-adjusted p-values below 0.05 are treated as positive detections, and precision and recall are computed accordingly. Further details on the computation of p-values for the PPI and UC methods are given in the supplementary materials.

To compute PR-AUC, regions are ranked by their continuous scores. For each threshold, we calculate the corresponding precision and recall values, and the PR-AUC is obtained as the area under the precision-recall curve. This provides a threshold-independent summary of detection performance. For our approach and PPI, precision, recall, and PR-AUC are computed using $s(r)$ and $s_{PPI}(r)$, respectively. For the UC analysis, where s_{UC} is a symmetric matrix, we use the elements of its vectorized upper-triangular part as a score for region pairs.

4.3. Results

Linear setting:: Figure 3 provides an illustration of our experiment’s results. The upper panel shows the observed test statistic $s(r)$ in red, along with the mean (orange) and standard deviation (purple) of the test statistics obtained from $B = 1000$ random permutations. The middle panel presents the distance-correlation matrices for X and Y . As expected, the main connectivity differences are concentrated within the first block. The regions exhibiting the highest values of $s(r)$ closely align with this altered cluster, clearly emphasizing the relevant features (indices 0–20). In contrast, the permuted statistics show no structural signal, confirming that the observed deviations are specific to the true connectivity differences.

To evaluate performance systematically, we repeated the simulation across a range of γ values, where larger γ induces stronger and more structured linear dependencies among the regions. Bottom panel of Figure 3 (left) depicts the PR-AUC as a function of γ . Although our method initially yields slightly lower PR-AUC at weak signal strengths, it improves rapidly and surpasses both competing approaches once $\gamma \approx 0.9$. This indicates that as the linear dependency structure strengthens, our framework more effectively prioritizes the truly relevant regions. Bottom panel, middle and right plots of Figure 3 show the precision and recall (after multiple-testing correction). While UC and PPI maintain relatively stable precision across all γ values, our method exhibits a steeper improvement, overtaking both for $\gamma > 1.3$. Regarding recall, UC performs best at low γ ($\approx 76\%$) but plateaus as the signal grows, whereas our approach continues to improve, approaching UC near $\gamma \approx 1.9$. PPI remains limited to about 40% recall due to its dependence on a single seed region, which constrains detection to a subset of affected clusters.

Non-linear setting:: Figure 4 provides an illustration of our results. As in the linear case, the top panel displays the observed $s(r)$ values against their

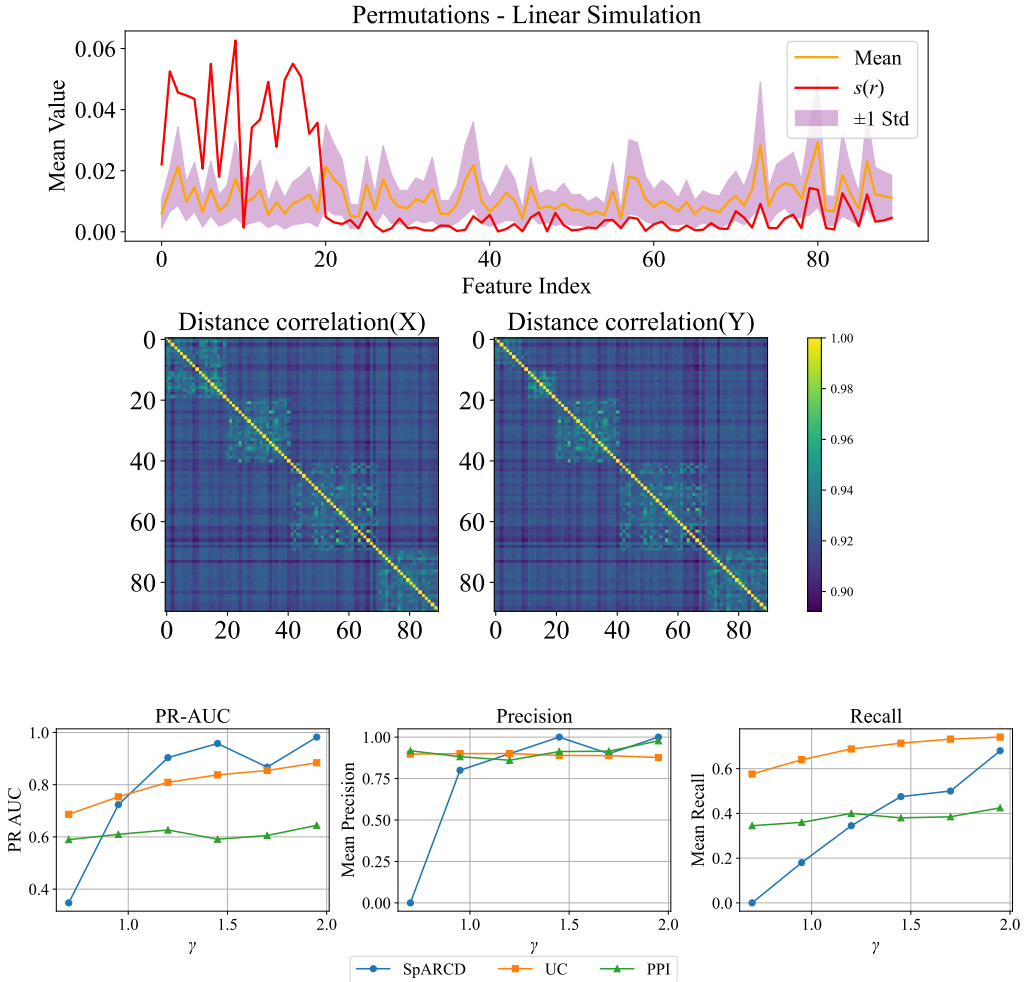


Figure 3: Linear simulation setting. **Top panel:** Observed test statistic $s(r)$ (red) compared with the mean (orange) and standard deviation (purple) of the permutation-based null distribution. **Middle panel:** Distance-correlation matrices for datasets X and Y , highlighting the regions with altered connectivity in the first cluster. **Bottom panel:** Performance of SpARCD and competing methods in the linear simulation setting with block-diagonal covariance structure. Precision (left), recall (middle), and PR-AUC (right) are shown as functions of the signal-strength parameter γ . Higher γ values correspond to stronger and more structured linear dependencies among clusters.

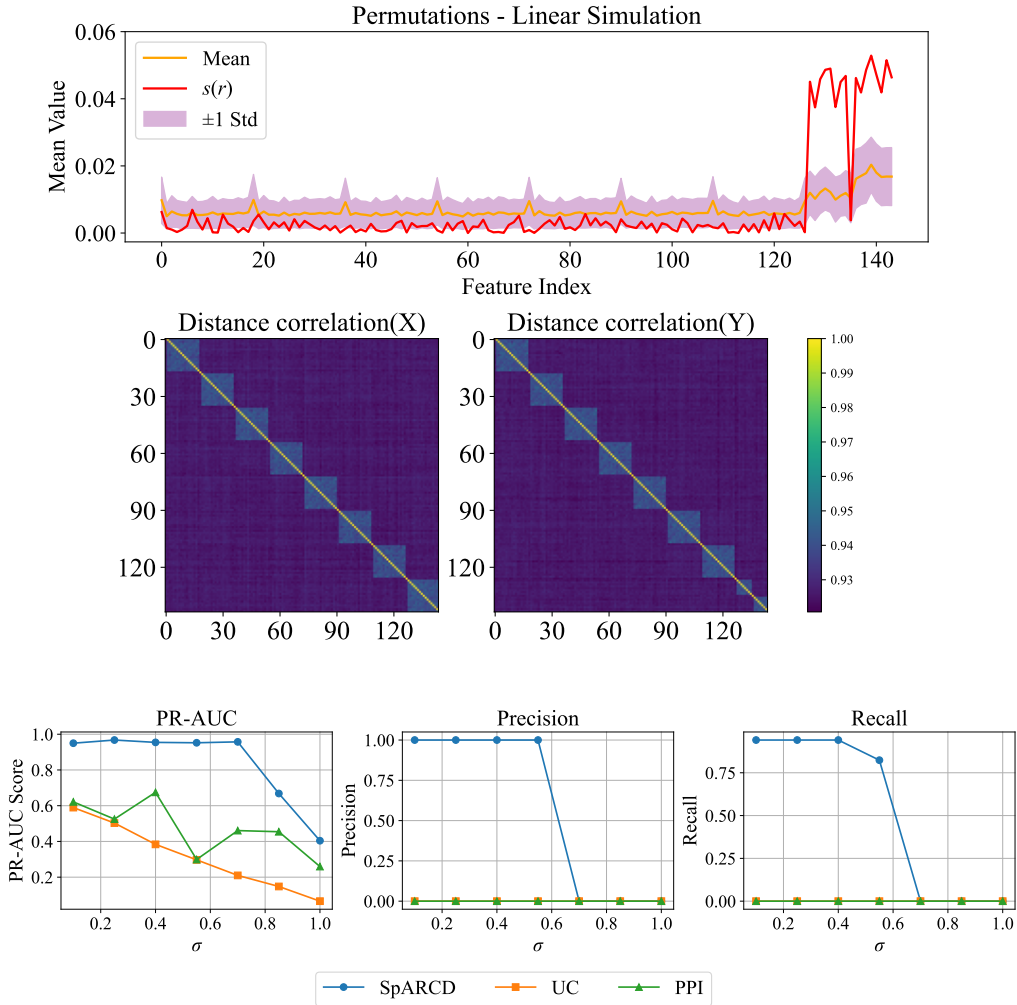


Figure 4: Nonlinear simulation setting. **Top panel:** Observed test statistic $s(r)$ (red) compared with the mean (orange) and standard deviation (purple) of the permutation-based null distribution. **Middle panel:** Distance-correlation matrices for datasets X and Y , demonstrating that the detected regions correspond to genuine nonlinear differences in connectivity. **Bottom panel:** Performance of SpARCD and competing methods in the nonlinear simulation setting under varying noise levels (σ). Precision (left), recall (middle), and PR-AUC (right) as functions of the noise level. The results show that SpARCD maintains high accuracy and robustness even as noise increases, whereas competing methods rapidly lose power after multiple-testing correction.

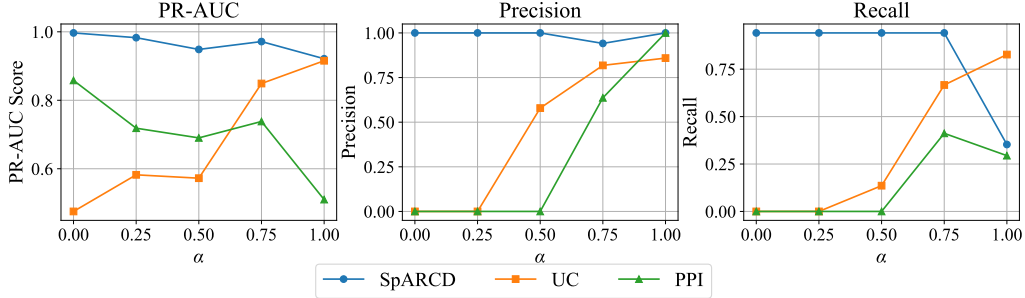


Figure 5: Performance of SpARCD and competing methods in the hybrid simulation setting with varying degrees of linearity (α). Precision (left), recall (middle), and PR-AUC (right) as functions of the mixing parameter α , where smaller values indicate stronger nonlinear effects. SpARCD achieves the best overall performance for low-to-moderate α , while maintaining competitive accuracy as dependencies become predominantly linear.

permutation-based null distribution. The discriminative signal is considerably clearer here: our test statistic highlights the differentiating regions with minimal background noise. The corresponding distance-correlation matrices further confirm that detected regions coincide with genuine connectivity changes between X and Y .

Bottom panel of Figure 4 summarizes the quantitative comparison. For increasing noise levels (σ), both PPI and UC exhibit moderate PR-AUC based on their raw outputs but yield no significant detections after multiple-testing correction, resulting in zero recall and precision across all σ . In contrast, our approach maintains perfect precision and recall up to $\sigma \approx 0.7$ and remains superior at higher noise levels, though with some expected performance degradation as the task becomes more challenging.

Hybrid setting. Figure 5 demonstrates that our method outperforms both baselines for low-to-moderate α , where nonlinear effects dominate. As α increases and dependencies become predominantly linear, UC gradually improves and slightly exceeds our recall for $\alpha \geq 0.8$. Nonetheless, our method retains high precision and strong overall performance across all regimes, reflecting its robustness to varying dependency structures. PPI remains consistently inferior, highlighting the limitation of seed-based inference in detecting distributed connectivity changes.

5. Application to the Hariri fMRI Dataset

We applied the proposed SpARCD framework and the competing methods to fMRI data collected under the EFMT, following the Hariri protocol (Hariri et al., 2002), from the cohort described in Ben-Zion et al. (2019). As detailed in Section 1.1, the dataset includes $n = 113$ participants diagnosed with PTSD at baseline, each performing alternating emotional-face and neutral-shape matching blocks. The preprocessed BOLD time series were parcellated into $R = 113$ ROIs using the Harvard–Oxford cortical and subcortical atlas. The mapping of brain regions through parcellation is detailed in the supplementary materials. To construct our dataset, we segment the BOLD time series into two categorized groups of intervals for each subject: one group corresponds to the emotional-stimulus blocks, while the other group corresponds to the neutral-stimulus blocks. This yields two paired sets of fMRI recordings, denoted by $X, Y \in \mathbb{R}^{n \times R \times T}$, where n, R , and T are the number of patients, ROIs, and time samples, respectively. To identify regions whose FC profiles differ between the two states, we computed the regional test statistic $s(r)$. Significance was assessed via a permutation test with $B = 2000$ block-level permutations that preserve within-block temporal structure, followed by BH correction at level 0.05.

Figure 6 (bottom) displays the empirical distribution of the test statistic across regions. The red curve represents the observed $s(r)$, while the blue curve and light-blue band are the mean and standard deviation of the permutation-based null distribution. Several regions exhibit marked deviations above the null expectation, indicating state-dependent alterations in FC.

After multiple-testing correction, SpARCD identified 10 significantly differentiating regions that primarily correspond to the bilateral lateral occipital cortex (44–45), cuneal cortex (62–63), temporal occipital fusiform cortex (76–77), occipital fusiform gyrus (78–79), and occipital pole (94–95) — areas within the posterior visual network. This constellation of posterior visual regions is consistent with prior studies implicating the visual association network in emotion perception and threat-related visual processing, reflecting integration between visual and limbic systems (Eklund et al., 2016; Barch et al., 2013).

Importantly, these results reflect changes in functional coupling rather than local activation amplitude, underscoring SpARCD’s ability to capture distributed network reorganization. To characterize the specific brain net-

works with which these regions exhibit altered connectivity, one can examine the operator L_d , which provides a descriptive summary of these changes, as demonstrated in Figure 6 top panel. In ongoing work, we plan to develop hierarchical FDR procedures to assign statistical significance to these network-level interpretations.

For comparison, we repeated the analysis using PPI and UC testing. PPI results (Table Appendix B) depended strongly on the selected seed region: when the right amygdala (region 108) was used as the seed, 46 significant connections were identified; using the left amygdala (region 109) yielded only 34, with limited overlap beyond the limbic regions. This variability underscores the seed-selection bias inherent in PPI and its reduced ability to detect distributed changes. The UC approach (Figure 8 and Table B.3) produced a dense pattern of significant edges, many overlapping with SpARCD’s findings, but it lacked spatial coherence and yielded numerous isolated detections after FDR correction. SpARCD, in contrast, identified compact and interpretable subnetworks, reducing false positives while preserving statistical power.

We utilized the SpARCD framework in two additional experiments within the EFMT setting, which are detailed in the supplementary materials. First, we repeated the earlier experiments on control subjects without a PTSD diagnosis. Second, we applied this approach to examine changes in connectivity between the EFMT scans and resting-state fMRI scans of subjects diagnosed with PTSD. These two additional experiments provide further insights into EFMT task design from a functional connectivity perspective.

Crucially, the spectral filtering inherent in SpARCD allows it to disentangle shared baseline connectivity from condition-specific differences, producing clearer, interpretable region-level significance maps than competing methods. The results thus demonstrate that spectral graph-based inference, when coupled with distance-correlation connectivity estimation, provides a powerful and principled means of detecting network-level dysfunctions in high-dimensional fMRI data.

6. Application to the Resting-State fMRI Dataset

We applied SpARCD to resting-state fMRI data. As described in Section 1.1, the dataset comprises 113 participants diagnosed with PTSD and 42 healthy controls. For each participant, the scan consists of $T = 300$ time points. Similarly to the previous experiment, the preprocessed BOLD

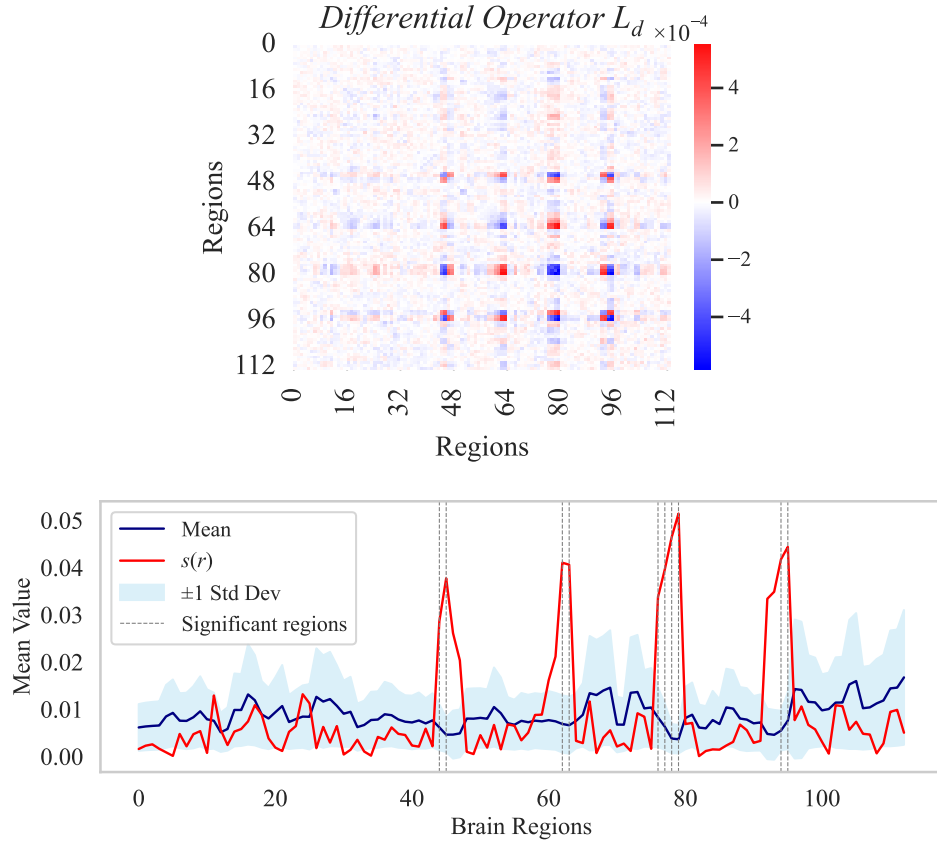


Figure 6: Results of SpARCD applied to the Hariri fMRI dataset. **Top:** The difference between the differential operators, L_d , on the Hariri fMRI dataset. **Bottom:** The observed test statistic $s(r)$ (red) is shown together with the mean (blue) and standard deviation (light blue) of the permutation-based null distribution. Several regions exhibit clear deviations above the null expectation, indicating significant differences in functional connectivity between the emotional and neutral task conditions.

time series were parcellated into $R = 113$ regions of interest (ROIs) according to the Harvard–Oxford cortical and subcortical atlas. In this experiments, our input consists of two *unpaired* datasets $X \in \mathbb{R}^{113 \times 113 \times 300}$ and $Y \in \mathbb{R}^{42 \times 113 \times 300}$, corresponding to the PTSD and control groups, respectively.

To identify regions exhibiting group-wise differences in FC profiles, we computed the regional test statistic $s(r)$. Statistical significance was assessed using a permutation test with $B = 2000$ permutations, followed by Benjamini–Hochberg correction at a false discovery rate of 0.05.

As shown in Figure 6, several regions demonstrate clear deviations above the null expectation, suggesting altered connectivity patterns in the PTSD group. After multiple-testing correction, SpARCD identified four regions with significant group-level differences, corresponding to the bilateral intracalcarine cortex (46–47) and cuneal cortex (62–63), which are located within the primary and higher-order visual areas, respectively.

This constellation of posterior visual regions is consistent with prior work linking abnormal visual network organization to hypervigilance and heightened sensory processing in PTSD (Leite et al., 2022). Moreover, our findings align with evidence implicating visual networks and the medial somatosensory network (MSN) in PTSD prediction and symptom expression (Ben-Zion et al., 2025). Prior work shows that altered visual processing is a core feature of PTSD (Fleming et al., 2024; Mueller-Pfeiffer et al., 2013) and that persistent trauma-related sensory memories can disrupt visual processing at preattentive stages (Hendler et al., 2003). Enhanced somatosensory–visual connectivity following trauma-focused psychotherapy has also been associated with better treatment outcomes (Korgaonkar et al., 2020). These results highlight the functional importance of visual-system circuitry in early PTSD and provide complementary support for the alterations detected by SpARCD.

The effects observed here further demonstrate SpARCD’s capacity to detect meaningful connectivity alterations in *unpaired* group-level comparisons, highlighting its flexibility beyond within-subject paradigms. These findings suggest that even at rest, PTSD may be characterized by atypical intrinsic coupling within the visual system, potentially reflecting altered sensory and attentional processing associated with the disorder.

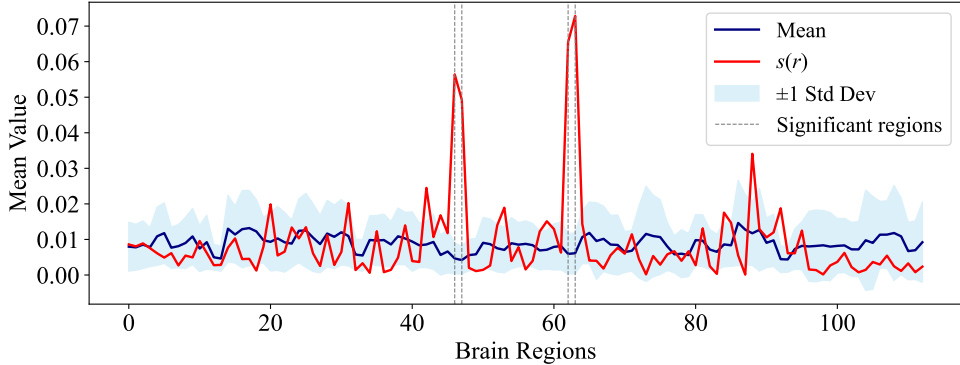


Figure 7: Results of SpARCD applied to the resting-state fMRI dataset. The observed test statistic $s(r)$ (red) is shown together with the mean (blue) and standard deviation (light blue) of the permutation-based null distribution. Several regions exhibit clear deviations above the null expectation, indicating significant differences in functional connectivity between PTSD subjects and controls.

7. Discussion

This work introduced SpARCD, a distance-correlation-based spectral framework for detecting differential functional connectivity between experimental conditions. By combining a nonlinear dependence measure with spectral graph filtering, SpARCD isolates structured, condition-specific changes in connectivity while suppressing shared baseline patterns. Through both simulations and empirical analysis of fMRI data, the method demonstrated high sensitivity and specificity in identifying distributed network alterations in paired and unpaired settings. The analysis was performed on EFMT (Hariri) and resting-state scans from PTSD and healthy patients, illustrating SpARCD’s ability to address different types of fMRI scans.

A central advantage of SpARCD lies in its ability to move beyond edge-wise testing toward network-level inference. Unlike traditional methods such as PPI or UC analysis, which test individual connections or seed-based interactions, SpARCD captures coherent, multi-regional connectivity shifts. The spectral projection step filters out components common to both conditions, thereby revealing only those eigenmodes that differ meaningfully between states. This mechanism yields compact, interpretable subnetworks and mitigates false positives arising from widespread but nonspecific fluctuations.

In simulations, SpARCD consistently outperformed baseline methods across linear, nonlinear, and hybrid dependency structures. The method was partic-

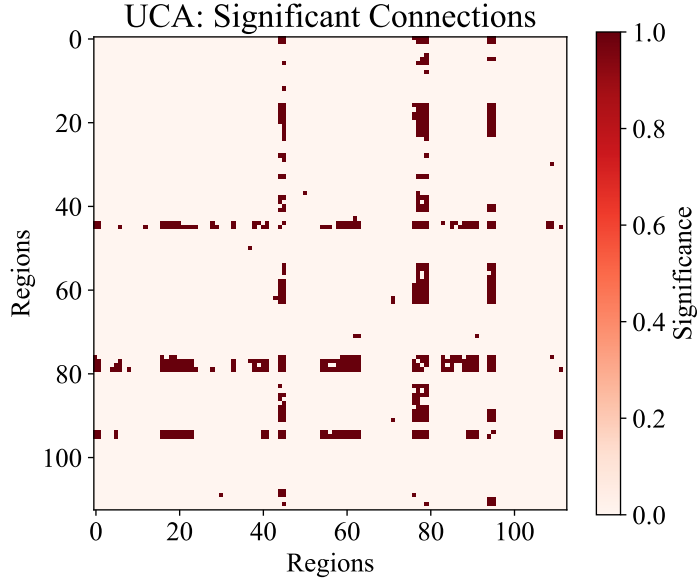


Figure 8: Results of the UC method applied to the Hariri fMRI dataset. Significant pairwise functional connections identified by the UC approach after BH multiple-testing correction. The detected edges show a dense but spatially fragmented pattern, illustrating the limited spatial coherence of UC compared with SpARCD.

ularly effective under nonlinear dependence, where classical correlation-based metrics lose power. These results highlight the value of distance correlation as a robust estimator of FC in complex neural systems.

When applied to the Hariri fMRI dataset, SpARCD uncovered a constellation of regions, predominantly within posterior visual areas, known to interact with limbic regions to support the processing of threat-related and emotional information. In the resting-state PTSD-control comparison, SpARCD identified posterior visual regions, including the intracalcarine and cuneal cortices, consistent with prior evidence of sensory-network dysregulation in PTSD. Even at rest, PTSD is characterized by atypical intrinsic coupling within early visual circuits, highlighting both the algorithm’s sensitivity and the functional relevance of these effects. Importantly, SpARCD detected these alterations through distributed connectivity changes rather than univariate activation differences, demonstrating its capacity to reveal subtle network-level dysregulation.

While the current study focused on binary condition comparisons, the

framework naturally extends to multi-state or longitudinal designs, and can incorporate subject-level covariates through hierarchical modeling of spectral scores. Mathematically, the difference operator or graph Laplacian used to define $s(r)$ can be extended to model multiple covariance structures or repeated measurements across time. Computational scalability is ensured by efficient Laplacian decomposition and the use of parallelized distance-correlation estimation. Future work may integrate SpARCD with causal or directed connectivity models, enabling inference on information flow rather than undirected association.

In summary, SpARCD provides a statistically principled and computationally tractable tool for studying connectivity alterations in high-dimensional neuroimaging data. Its general formulation makes it broadly applicable to other domains involving structured, multivariate dependence—such as genomics, climate networks, or financial systems, where uncovering subtle, distributed differences between complex systems is of primary interest.

Appendix A. Example Appendix Section

Appendix B. Details on PPI and univariate covariance analysis.

This section provides additional details on the psychophysiological interaction (PPI) analysis and univariate covariance comparisons used as benchmarks for the proposed SpARCD method. Table [Appendix B](#) summarizes the brain regions that exhibited significant task-dependent connectivity with predefined seed regions under the PPI framework, and Table [B.3](#) presents the results of the univariate covariance (UC) analysis.

PPI. The psychophysiological interaction (PPI) approach ([Friston et al., 1997](#)) is a classical technique for identifying task-dependent changes in functional connectivity. PPI models the interaction between a psychological variable (task design) and a physiological variable (the BOLD signal from a predefined seed region) within a general linear model (GLM) framework. Formally, for each brain region $y(t)$, the model is:

$$y(t) = \beta_0 + \beta_1 s(t) + \beta_2 p(t) + \beta_3 [s(t) \cdot p(t)] + \varepsilon(t),$$

where $s(t)$ denotes the seed region's time series (physiological regressor), $p(t)$ represents the psychological task regressor (e.g., emotional vs. neutral condition, convolved with the hemodynamic response function), and $s(t) \cdot p(t)$

is their interaction term. The coefficient β_3 quantifies the task-dependent modulation of connectivity between the seed and each target region. In our implementation, we computed the PPI regressor for each subject and seed region using the `nilearn` and `statsmodels` Python packages. The design matrix included the task, seed, and PPI terms, and a separate GLM was fitted for each target region. Group-level effects were assessed via one-sample t -tests across subjects, followed by FDR correction for multiple comparisons. Regions with FDR-corrected $p < 0.05$ were identified as exhibiting significant task-modulated connectivity with the seed.

Univariate correlation analysis. As an additional baseline, we performed a univariate correlation (UC) analysis to identify individual ROI-to-ROI connections that exhibit significant within-subject differences in functional connectivity across task conditions. For each subject and condition, we computed the Pearson correlation matrix of the BOLD time series across all regions, followed by Fisher’s z -transformation to stabilize variance. The upper-triangular elements of each correlation matrix were then extracted, and paired-sample t -tests were conducted across subjects for each connection to assess condition-related differences. Multiple comparison correction was performed using the Benjamini–Hochberg FDR procedure ($\alpha = 0.05$). Connections with FDR-corrected $p < 0.05$ were considered significant and were mapped back to their corresponding ROI pairs to form a binary significance matrix.

Table B.3: Significant ROI-to-ROI connections after FDR correction.

ROI	Connected ROIs
0	44, 45, 76, 77, 78, 79, 94, 95
1	44, 45, 77, 78, 79, 94, 95
4	79
5	78, 79, 94, 95
6	45, 77, 78, 79
8	79
12	45
16	44, 45, 76, 77, 78, 79, 94, 95
17	44, 45, 77, 78, 79, 94, 95

Continued on next page

Table B.3: Significant ROI-to-ROI connections after FDR correction.

ROI	Connected ROIs
18	44, 45, 76, 77, 78, 79, 94, 95
19	44, 45, 76, 77, 78, 79, 94, 95
20	44, 45, 77, 78, 79, 94, 95
21	45, 77, 78, 79, 94, 95
22	45, 77, 78, 79, 94, 95
23	45, 77, 78, 79, 94, 95
24	45, 79
28	44, 45, 79
29	45
30	109
33	44, 45, 77, 78, 79
37	50, 77
38	44, 45, 77, 78, 79
39	44, 77, 79
40	45, 77, 78, 79, 94, 95
41	44, 45, 77, 78, 79, 94, 95
43	62
44	0, 1, 16, 17, 18, 19, 20, 28, 33, 38, 39, 41, 45, 58, 59, 60, 61, 62, 63, 76, 77, 78, 79, 83, 85, 86, 88, 89, 90, 91, 94, 95, 108, 109
45	0, 1, 6, 12, 16, 17, 18, 19, 20, 21, 22, 23, 24, 28, 29, 33, 38, 40, 41, 44, 54, 55, 56, 58, 59, 60, 61, 62, 63, 76, 77, 78, 79, 85, 87, 88, 89, 90, 91, 94, 95, 108, 109, 111
50	37
54	45, 77, 78, 79, 94, 95
55	45, 77, 78, 79, 94, 95
56	45, 77, 79, 95
57	77, 79, 94, 95
58	44, 45, 77, 78, 79, 94, 95
59	44, 45, 76, 77, 78, 79, 94, 95
60	44, 45, 76, 77, 78, 79, 94, 95
61	44, 45, 76, 77, 78, 79, 94, 95
62	43, 44, 45, 71, 76, 77, 78, 79, 94, 95
63	44, 45, 71, 76, 77, 78, 79, 94, 95
71	62, 63, 91
76	0, 16, 18, 19, 44, 45, 59, 60, 61, 62, 63, 77, 78, 79, 83, 85, 86, 87, 89, 90, 91, 94, 95, 109
77	0, 1, 6, 16, 17, 18, 19, 20, 21, 22, 23, 33, 37, 38, 39, 40, 41, 44, 45, 54, 55, 56, 57, 58, 59, 60, 61, 62, 63, 76, 78, 79, 83, 84, 85, 86, 87, 88, 89, 90, 91, 94, 95
78	0, 1, 5, 6, 16, 17, 18, 19, 20, 21, 22, 23, 33, 38, 40, 41, 44, 45, 54, 55, 58, 59, 60, 61, 62, 63, 76, 77, 79, 83, 85, 88, 89, 90, 91, 94, 95

Continued on next page

Table B.3: Significant ROI-to-ROI connections after FDR correction.

ROI	Connected ROIs
79	0, 1, 4, 5, 6, 8, 16, 17, 18, 19, 20, 21, 22, 23, 24, 28, 33, 38, 39, 40, 41, 44, 45, 54, 55, 56, 57, 58, 59, 60, 61, 62, 63, 76, 77, 78, 83, 84, 85, 88, 89, 90, 91, 94, 95, 111
83	44, 76, 77, 78, 79
84	77, 79
85	44, 45, 76, 77, 78, 79
86	44, 76, 77
87	45, 76, 77
88	44, 45, 77, 78, 79
89	44, 45, 76, 77, 78, 79, 94, 95
90	44, 45, 76, 77, 78, 79, 94, 95
91	44, 45, 71, 76, 77, 78, 79, 94, 95
94	0, 1, 5, 16, 17, 18, 19, 20, 21, 22, 23, 40, 41, 44, 45, 54, 55, 57, 58, 59, 60, 61, 62, 63, 76, 77, 78, 79, 89, 90, 91, 95, 110, 111
95	0, 1, 5, 16, 17, 18, 19, 20, 21, 22, 23, 40, 41, 44, 45, 54, 55, 56, 57, 58, 59, 60, 61, 62, 63, 76, 77, 78, 79, 89, 90, 91, 94, 110, 111
108	44, 45
109	30, 44, 45, 76
110	94, 95
111	45, 79, 94, 95

Appendix C. Additional Experiments on fMRI Connectivity

In addition to the primary EFMT analysis in PTSD patients (Section 5), we conducted two supplementary experiments to evaluate the robustness and generalizability of our method on EFMT data. In all cases, we compute connectivity graphs for the two states A and B , apply the spectral differential operator, and calculate the regional test statistic $s(r)$ as described in the main text.

Face vs. Shape in Healthy Subjects. We applied the proposed SpARCD framework to EFMT data from the subset of healthy participants in the cohort described in Section 1.1 ($n = 47$). The preprocessing, ROI parcelation, and block structure are identical to those described for the PTSD cohort in Section 5. For each participant, we constructed paired datasets $X, Y \in \mathbb{R}^{n \times 113 \times 68}$ corresponding to the face (A) and shape (B) blocks of the EFMT. We then computed the regional test statistic $s(r)$, and significance

Table B.2: Summary of PPI results by seed.

Seed 0	35 43 44 45 77 79 94
Seed 13	0 24 40 45 51 61 76 77 78 79 90
Seed 77	0 1 2 3 4 5 6 7 8 9 10 11 12 13 14 15 16 17 18 19 20 21 22 23 24 25 26 27 28 29 30 31 32 33 34 35 36 37 38 39 40 41 42 43 45 46 47 48 50 51 52 53 54 55 56 57 58 59 60 61 62 63 64 65 66 67 68 69 70 71 72 73 74 75 78 79 80 81 82 83 84 85 86 87 88 89 90 91 92 93 94 95 96 97 98 99 100 101 102 103 104 105 106 107 108 110 111 112
Seed 108	0 11 16 18 20 21 22 23 24 28 30 31 35 43 44 45 54 55 56 57 58 59 60 70 71 76 77 78 79 94 95 97 106 111
Seed 109	0 1 2 5 11 15 16 17 18 19 20 21 22 23 26 27 28 30 31 43 44 45 54 55 56 57 58 59 60 61 70 71 73 76 77 78 79 84 85 86 87 94 95 97 110 111
Seed 112	-

was assessed via permutation test ($B = 2000$) as described in Step IV Section 1.1 with BH correction at $\alpha = 0.05$. The results were broadly consistent with those obtained for the PTSD cohort. Regions $\{44, 45, 76, 77, 78, 79, 94, 95\}$ exhibited significant connectivity differences, overlapping substantially with those identified in PTSD participants. In contrast, regions $\{62, 63\}$ did not reach statistical significance in the healthy group.

Overall, these findings indicate that the connectivity differences between face and shape blocks are largely similar between PTSD and healthy participants, suggesting that the pattern of task-evoked connectivity is largely preserved across these groups.

EFMT vs. Resting-State fMRI in PTSD Subjects. We compared task-based connectivity during the EFMT to resting-state connectivity within the PTSD cohort described in Section 1.1 ($n = 113$). The preprocessing and ROI parcellation were identical to the main analysis. To match time series lengths, the edges of the resting-state scans were truncated. For each participant, we constructed paired datasets $X, Y \in \mathbb{R}^{n \times 113 \times T}$ corresponding to EFMT (X) and resting-state (Y) signals. We then computed the test statistic $s(r)$, with statistical significance evaluated by a standard permutation test ($B = 5000$)

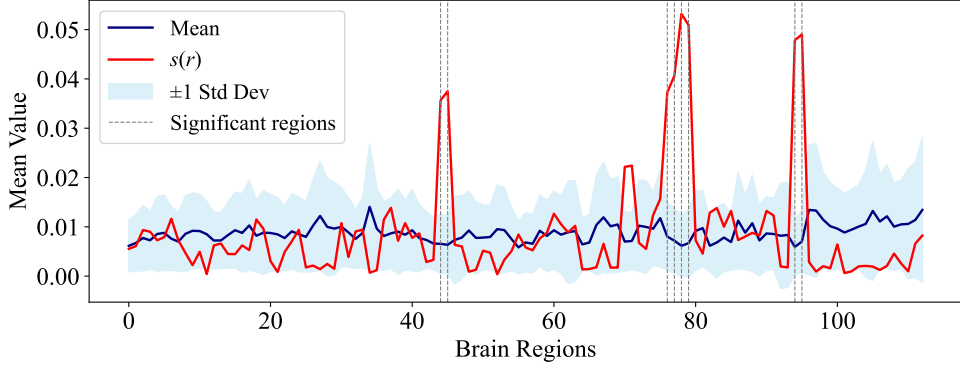


Figure C.9: Results of the SpARCD analysis applied to the Hariri fMRI dataset for the non-PTSD patient cohort. The observed test statistic $s(r)$ (red) is shown together with the mean (blue) and standard deviation (light blue) of the permutation-based null distribution. Several regions exhibit clear deviations above the null expectation, indicating significant differences in functional connectivity between the emotional and neutral task conditions.

followed by BH correction at $\alpha = 0.05$.

In this analysis, most of the identified regions are subsets of those found in the comparison between emotional and neutral stimuli. Regions [62 63 77 78 79 94 95]{62, 63, 77, 78, 79, 92, 93, 94, 95} showed significant differences in connectivity. Notably, regions {92, 93} were previously unidentified. In contrast, regions {44, 45} did not achieve statistical significance in this comparison.

A visual inspection of the $s(r)$ profiles reveals that the elevated $s(r)$ values are still apparent in the unidentified regions when compared to the permuted distributions. This suggests that the discrepancies are likely due to a higher variance in the permuted statistic, $\tilde{s}(r)$. This higher variance may occur because we are permuting between two distinctly different scan types.

Appendix D. Data-driven estimation of the hyperparameter K

The hyperparameter K controls the number of leading eigenvectors included in the construction of the projection operators Q_X and Q_Y (Step II, Section 3), thereby determining the spectral resolution at which connectivity structures are compared. Selecting too few eigenvectors (small K) retains too much shared structure between the graphs, potentially masking region-specific differences. Conversely, selecting too many eigenvectors (large K)

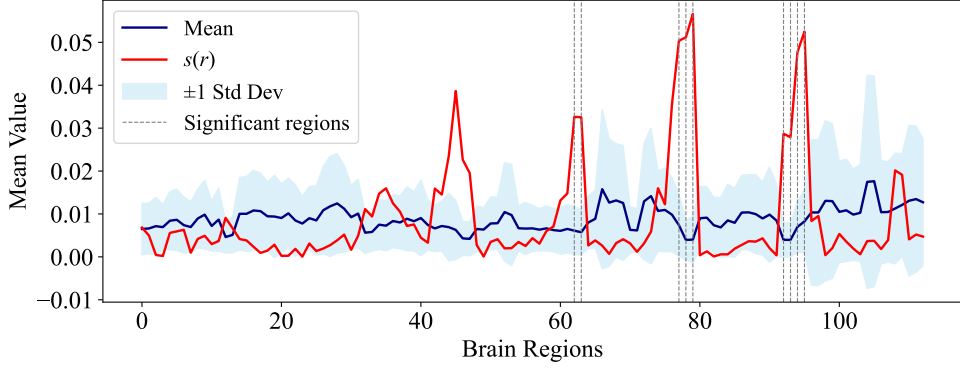


Figure C.10: Results of SpARCD for the comparison of the Hariri fMRI dataset and resting-state fMRI on PTSD patients.

The observed test statistic $s(r)$ (red) is shown together with the mean (blue) and standard deviation (light blue) of the permutation-based null distribution. Several regions exhibit clear deviations above the null expectation, indicating significant differences in functional connectivity between the emotional and neutral task conditions.

removes most of the dominant connectivity patterns, leaving mostly noise and reducing the meaningfulness of the resulting test statistic.

To guide the choice of K , we adopt a data-driven criterion that reflects the magnitude of regional differences captured by the test statistic $s(r)$. Recall that $s(r)$ is derived from the leading eigenvector v_d of the differential operator and is defined as,

$$s(r) = \frac{|v_d(r)|}{\|v_d\|_1}, \quad \text{with } \|v_d\|_2 = 1.$$

A concentrated $s(r)$ indicates strong localized differences in connectivity, while a more uniform $s(r)$ suggests weaker or diffuse differences.

For each candidate $K \in \{1, 2, \dots, R\}$, we compute $s^{(K)}(r)$ on the data, and evaluate its ℓ_2 norm: $\eta(K) = \|s^{(K)}\|_2$. Since $\|s^{(K)}\|_1 = 1$ by construction, $\eta(K)$ serves as a measure of imbalance or sparsity in $s^{(K)}$: higher values correspond to more pronounced contrast among regions. We then select $K^* = \arg \max_K \eta(K)$, which yields the spectral resolution that maximizes regional differentiation between the two states.

In practice, we restrict K to the range $2 \leq K \leq 80$ to avoid under- or over-filtering. This range was determined empirically based on the total number of eigenvalues (113) in our Laplacian matrices. For the permutation

test (Step IV, Section 3), K^* is re-estimated separately for each permuted dataset to maintain the validity of the procedure.

Appendix E. Atlas-ROI mapping

A mapping of ROI numbers to their corresponding anatomical names.

Table E.4: Mapping between ROI indices and brain region names (Harvard-Oxford Atlas).

ROI Index	Brain Region
0	Left Frontal Pole
1	Right Frontal Pole
2	Left Insular Cortex
3	Right Insular Cortex
4	Left Superior Frontal Gyrus
5	Right Superior Frontal Gyrus
6	Left Middle Frontal Gyrus
7	Right Middle Frontal Gyrus
8	Left Inferior Frontal Gyrus pars triangularis
9	Right Inferior Frontal Gyrus pars triangularis
10	Left Inferior Frontal Gyrus pars opercularis
11	Right Inferior Frontal Gyrus pars opercularis
12	Left Right Precentral Gyrus
13	Right Precentral Gyrus
14	Left Temporal Pole
15	Right Temporal Pole
16	Left Superior Temporal Gyrus anterior division
17	Right Superior Temporal Gyrus anterior division
18	Left Superior Temporal Gyrus posterior division
19	Right Superior Temporal Gyrus posterior division
20	Left Middle Temporal Gyrus anterior division
21	Right Middle Temporal Gyrus anterior division
22	Left Middle Temporal Gyrus posterior division
23	Right Middle Temporal Gyrus posterior division
24	Left Middle Temporal Gyrus temporooccipital part

Continued on next page

Table E.4: Mapping between ROI indices and brain region names (Harvard-Oxford Atlas).

ROI Index	Brain Region
25	Right Middle Temporal Gyrus temporooccipital part
26	Left Inferior Temporal Gyrus anterior division
27	Right Inferior Temporal Gyrus anterior division
28	Left Inferior Temporal Gyrus posterior division
29	Right Inferior Temporal Gyrus posterior division
30	Left Inferior Temporal Gyrus temporooccipital part
31	Right Inferior Temporal Gyrus temporooccipital part
32	Left Postcentral Gyrus
33	Right Postcentral Gyrus
34	Left Superior Parietal Lobule
35	Right Superior Parietal Lobule
36	Left Supramarginal Gyrus anterior division
37	Right Supramarginal Gyrus anterior division
38	Left Supramarginal Gyrus posterior division
39	Right Supramarginal Gyrus posterior division
40	Left Angular Gyrus
41	Right Angular Gyrus
42	Left Lateral Occipital Cortex superior division
43	Right Lateral Occipital Cortex superior division
44	Left Lateral Occipital Cortex inferior division
45	Right Lateral Occipital Cortex inferior division
46	Left Intracalcarine Cortex
47	Right Intracalcarine Cortex
48	Left Frontal Medial Cortex
49	Right Frontal Medial Cortex
50	Left Juxtapositional Lobule Cortex (formerly Supplementary Motor Cortex)
51	Right Juxtapositional Lobule Cortex (formerly Supplementary Motor Cortex)
52	Left Subcallosal Cortex
53	Right Subcallosal Cortex
54	Left Paracingulate Gyrus
55	Right Paracingulate Gyrus
56	Left Cingulate Gyrus anterior division
57	Right Cingulate Gyrus anterior division

Continued on next page

Table E.4: Mapping between ROI indices and brain region names (Harvard-Oxford Atlas).

ROI Index	Brain Region
58	Left Cingulate Gyrus posterior division
59	Right Cingulate Gyrus posterior division
60	Left Precuneous Cortex
61	Right Precuneous Cortex
62	Left Cuneal Cortex
63	Right Cuneal Cortex
64	Left Frontal Orbital Cortex
65	Right Frontal Orbital Cortex
66	Left Parahippocampal Gyrus anterior division
67	Right Parahippocampal Gyrus anterior division
68	Left Parahippocampal Gyrus posterior division
69	Right Parahippocampal Gyrus posterior division
70	Left Lingual Gyrus
71	Right Lingual Gyrus
72	Left Temporal Fusiform Cortex anterior division
73	Right Temporal Fusiform Cortex anterior division
74	Left Temporal Fusiform Cortex posterior division
75	Right Temporal Fusiform Cortex posterior division
76	Left Temporal Occipital Fusiform Cortex
77	Right Temporal Occipital Fusiform Cortex
78	Left Occipital Fusiform Gyrus
79	Right Occipital Fusiform Gyrus
80	Left Frontal Operculum Cortex
81	Right Frontal Operculum Cortex
82	Left Central Opercular Cortex
83	Right Central Opercular Cortex
84	Left Parietal Operculum Cortex
85	Right Parietal Operculum Cortex
86	Left Planum Polare
87	Right Planum Polare
88	Left Heschls Gyrus (includes H1 and H2)
89	Right Heschls Gyrus (includes H1 and H2)
90	Left Planum Temporale

Continued on next page

Table E.4: Mapping between ROI indices and brain region names (Harvard-Oxford Atlas).

ROI Index	Brain Region
91	Right Planum Temporale
92	Left Supracalcarine Cortex
93	Right Supracalcarine Cortex
94	Left Occipital Pole
95	Right Occipital Pole
96	Left Lateral Ventricle
97	Right Lateral Ventricle
98	Left Thalamus
99	Right Thalamus
100	Left Caudate
101	Right Caudate
102	Left Putamen
103	Right Putamen
104	Left Pallidum
105	Right Pallidum
106	Left Hippocampus
107	Right Hippocampus
108	Left Amygdala
109	Right Amygdala
110	Left Accumbens
111	Right Accumbens
112	Brain-Stem

References

Anand, A., Li, Y., Wang, Y., Wu, J., Gao, S., Bukhari, L., Mathews, V.P., Kalnin, A., Lowe, M.J., 2005. Activity and connectivity of brain mood regulating circuit in depression: a functional magnetic resonance study. *Biological psychiatry* 57, 1079–1088.

Barch, D.M., Burgess, G.C., Harms, M.P., Petersen, S.E., Schlaggar, B.L., Corbetta, M., Glasser, M.F., Curtiss, S., Dixit, S., Feldt, C., et al., 2013.

Function in the human connectome: task-fmri and individual differences in behavior. *Neuroimage* 80, 169–189.

Belkin, M., Niyogi, P., 2003. Laplacian eigenmaps for dimensionality reduction and data representation. *Neural computation* 15, 1373–1396.

Ben Simon, E., Maron-Katz, A., Lahav, N., Shamir, R., Hendler, T., 2017. Tired and misconnected: a breakdown of brain modularity following sleep deprivation. *Human brain mapping* 38, 3300–3314.

Ben-Zion, Z., Fine, N.B., Keynan, N.J., Admon, R., Halpern, P., Liberzon, I., Hendler, T., Shalev, A.Y., 2019. Neurobehavioral moderators of post-traumatic stress disorder (ptsd) trajectories: study protocol of a prospective mri study of recent trauma survivors. *European Journal of Psychotraumatology* 10, 1683941.

Ben-Zion, Z., Simon, A.J., Rosenblatt, M., Korem, N., Duek, O., Liberzon, I., Shalev, A.Y., Hendler, T., Levy, I., Harpaz-Rotem, I., et al., 2025. Connectome-based predictive modeling of ptsd development among recent trauma survivors. *JAMA network open* 8, e250331–e250331.

Bullmore, E., Sporns, O., 2009. Complex brain networks: graph theoretical analysis of structural and functional systems. *Nature reviews neuroscience* 10, 186–198.

Cahill, N.D., Singh, H., Zhang, C., Corcoran, D.A., Prengaman, A.M., Wenger, P.S., Hamilton, J.F., Bajorski, P., Michael, A.M., 2016. Multiple-view spectral clustering for group-wise functional community detection. *arXiv preprint arXiv:1611.06981* .

Carballido, A., Scheuerecker, J., Meisenzahl, E., Schoepf, V., Bokde, A., Möller, H.J., Doyle, M., Wiesmann, M., Frodl, T., 2011. Functional connectivity of emotional processing in depression. *Journal of affective disorders* 134, 272–279.

Chung, F.R.K., 1997. Spectral Graph Theory. volume 92. American Mathematical Society.

Coifman, R.R., Lafon, S., 2006. Diffusion maps. *Applied and computational harmonic analysis* 21, 5–30.

Craddock, R.C., James, G.A., Holtzheimer III, P.E., Hu, X.P., Mayberg, H.S., 2012. A whole brain fmri atlas generated via spatially constrained spectral clustering. *Human brain mapping* 33, 1914–1928.

Cribben, I., Yu, Y., 2017. Estimating whole-brain dynamics by using spectral clustering. *Journal of the Royal Statistical Society Series C: Applied Statistics* 66, 607–627.

Crossley, N.A., Mechelli, A., Vértes, P.E., Winton-Brown, T.T., Patel, A.X., Ginestet, C.E., McGuire, P., Bullmore, E.T., 2013. Cognitive relevance of the community structure of the human brain functional coactivation network. *Proceedings of the National Academy of Sciences* 110, 11583–11588.

Daudt, R.C., Le Saux, B., Boulch, A., Gousseau, Y., 2018. Urban change detection for multispectral earth observation using convolutional neural networks, in: IGARSS 2018-2018 IEEE International Geoscience and Remote Sensing Symposium, Ieee. pp. 2115–2118.

Eklund, A., Nichols, T.E., Knutsson, H., 2016. Cluster failure: Why fmri inferences for spatial extent have inflated false-positive rates. *Proceedings of the national academy of sciences* 113, 7900–7905.

Etkin, A., Wager, T.D., 2007. Functional neuroimaging of anxiety: a meta-analysis of emotional processing in ptsd, social anxiety disorder, and specific phobia. *American journal of Psychiatry* 164, 1476–1488.

Finn, E.S., Shen, X., Scheinost, D., Rosenberg, M.D., Huang, J., Chun, M.M., Papademetris, X., Constable, R.T., 2015. Functional connectome fingerprinting: identifying individuals using patterns of brain connectivity. *Nature neuroscience* 18, 1664–1671.

Fleming, L.L., Harnett, N.G., Ressler, K.J., 2024. Sensory alterations in post-traumatic stress disorder. *Current Opinion in Neurobiology* 84, 102821.

Friston, K.J., Buechel, C., Fink, G.R., Morris, J., Rolls, E., Dolan, R.J., 1997. Psychophysiological and modulatory interactions in neuroimaging. *NeuroImage* 6, 218–229. doi:[10.1006/nimg.1997.0291](https://doi.org/10.1006/nimg.1997.0291).

Gerchen, M.F., Bernal-Casas, D., Kirsch, P., 2014. Analyzing task-dependent brain network changes by whole-brain psychophysiological interactions: A comparison to conventional analysis. *Human brain mapping* 35, 5071–5082.

Goghari, V.M., Sanford, N., Spilka, M.J., Woodward, T.S., 2017. Task-related functional connectivity analysis of emotion discrimination in a family study of schizophrenia. *Schizophrenia bulletin* 43, 1348–1362.

Gorka, S.M., Fitzgerald, D.A., King, A.C., Phan, K.L., 2013. Alcohol attenuates amygdala–frontal connectivity during processing social signals in heavy social drinkers: A preliminary pharmacofMRI study. *Psychopharmacology* 229, 141–154.

Greicius, M.D., Srivastava, G., Reiss, A.L., Menon, V., 2004. Default-mode network activity distinguishes Alzheimer's disease from healthy aging: evidence from functional MRI. *Proceedings of the National Academy of Sciences* 101, 4637–4642.

Hariri, A.R., Tessitore, A., Mattay, V.S., Fera, F., Weinberger, D.R., 2002. The amygdala response to emotional stimuli: a comparison of faces and scenes. *Neuroimage* 17, 317–323.

Hendler, T., Rotshtein, P., Yeshurun, Y., Weizmann, T., Kahn, I., Ben-Bashat, D., Malach, R., Bleich, A., 2003. Sensing the invisible: differential sensitivity of visual cortex and amygdala to traumatic context. *Neuroimage* 19, 587–600.

Jacob, Y., Shany, O., Goldin, P., Gross, J., Hendler, T., 2019. Reappraisal of interpersonal criticism in social anxiety disorder: a brain network hierarchy perspective. *Cerebral cortex* 29, 3154–3167.

Jacob, Y., Winetraub, Y., Raz, G., Ben-Simon, E., Okon-Singer, H., Rosenberg-Katz, K., Hendler, T., Ben-Jacob, E., 2016. Dependency network analysis (depna) reveals context related influence of brain network nodes. *Scientific Reports* 6, 27444.

Korgaonkar, M.S., Chakouch, C., Breukelaar, I.A., Erlinger, M., Felmingham, K.L., Forbes, D., Williams, L.M., Bryant, R.A., 2020. Intrinsic connectomes underlying response to trauma-focused psychotherapy in post-traumatic stress disorder. *Translational psychiatry* 10, 270.

Leite, L., Esper, N.B., Junior, J.R.M.L., Lara, D.R., Buchweitz, A., 2022. An exploratory study of resting-state functional connectivity of amygdala subregions in posttraumatic stress disorder following trauma in adulthood. *Scientific Reports* 12, 9558.

Li, M.T., Sun, J.W., Zhan, L.L., Antwi, C.O., Lv, Y.T., Jia, X.Z., Ren, J., 2023. The effect of seed location on functional connectivity: evidence from an image-based meta-analysis. *Frontiers in Neuroscience* 17, 1120741.

Liao, W., Zhang, Z., Pan, Z., Mantini, D., Ding, J., Duan, X., Luo, C., Lu, G., Chen, H., 2010. Altered functional connectivity and small-world in mesial temporal lobe epilepsy. *PloS one* 5, e8525.

Logothetis, N.K., 2008. What we can do and what we cannot do with fmri. *Nature* 453, 869–878.

Love, M.I., Huber, W., Anders, S., 2014. Moderated estimation of fold change and dispersion for rna-seq data with deseq2. *Genome biology* 15, 550.

McLaren, D.G., Ries, M.L., Xu, G., Johnson, S.C., 2012. A generalized form of context-dependent psychophysiological interactions (gppi): A comparison to standard approaches. *NeuroImage* 61, 1277–1286. doi:[10.1016/j.neuroimage.2012.03.068](https://doi.org/10.1016/j.neuroimage.2012.03.068).

Mohanty, R., Sethares, W.A., Nair, V.A., Prabhakaran, V., 2020. Rethinking measures of functional connectivity via feature extraction. *Scientific reports* 10, 1298.

Mueller-Pfeiffer, C., Schick, M., Schulte-Vels, T., O’Gorman, R., Michels, L., Martin-Soelch, C., Blair, J.R., Rufer, M., Schnyder, U., Zeffiro, T., et al., 2013. Atypical visual processing in posttraumatic stress disorder. *NeuroImage: Clinical* 3, 531–538.

Ng, A., Jordan, M., Weiss, Y., 2001. On spectral clustering: Analysis and an algorithm. *Advances in neural information processing systems* 14.

Nichols, T., Hayasaka, S., 2003. Controlling the familywise error rate in functional neuroimaging: a comparative review. *Statistical methods in medical research* 12, 419–446.

O'daly, O.G., Trick, L., Scaife, J., Marshall, J., Ball, D., Phillips, M.L., Williams, S.S., Stephens, D.N., Duka, T., 2012. Withdrawal-associated increases and decreases in functional neural connectivity associated with altered emotional regulation in alcoholism. *Neuropsychopharmacology* 37, 2267–2276.

Sanz-Arigita, E.J., Schoonheim, M.M., Damoiseaux, J.S., Rombouts, S.A., Maris, E., Barkhof, F., Scheltens, P., Stam, C.J., 2010. Loss of 'small-world' networks in alzheimer's disease: graph analysis of fmri resting-state functional connectivity. *PloS one* 5, e13788.

Savage, H.S., Mulders, P.C., Van Eijndhoven, P.F., Van Oort, J., Tendolkar, I., Vrijen, J.N., Beckmann, C.F., Marquand, A.F., 2024. Dissecting task-based fmri activity using normative modelling: an application to the emotional face matching task. *Communications biology* 7, 888.

Shen, X., Tokoglu, F., Papademetris, X., Constable, R.T., 2013. Group-wise whole-brain parcellation from resting-state fmri data for network node identification. *Neuroimage* 82, 403–415.

Shin, L.M., Liberzon, I., 2010. The neurocircuitry of fear, stress, and anxiety disorders. *Neuropsychopharmacology* 35, 169–191.

Smith, D.V., Gseir, M., Speer, M.E., Delgado, M.R., 2016. Toward a cumulative science of functional integration: A meta-analysis of psychophysiological interactions. *Human brain mapping* 37, 2904–2917.

Smith, S.M., Fox, P.T., Miller, K.L., Glahn, D.C., Fox, P.M., Mackay, C.E., Filippini, N., Watkins, K.E., Toro, R., Laird, A.R., et al., 2009. Correspondence of the brain's functional architecture during activation and rest. *Proceedings of the national academy of sciences* 106, 13040–13045.

Smyth, G.K., 2004. Linear models and empirical bayes methods for assessing differential expression in microarray experiments. *Statistical applications in genetics and molecular biology* 3.

Sripada, R.K., King, A.P., Welsh, R.C., Garfinkel, S.N., Wang, X., Sripada, C.S., Liberzon, I., 2012. Neural dysregulation in posttraumatic stress disorder: evidence for disrupted equilibrium between salience and default mode brain networks. *Biopsychosocial Science and Medicine* 74, 904–911.

Sristi, R.D., Mishne, G., Jaffe, A., 2022. Disc: Differential spectral clustering of features. *Advances in Neural Information Processing Systems* 35, 26269–26282.

Székely, G.J., Rizzo, M.L., Bakirov, N.K., 2007. Measuring and testing dependence by correlation of distances. *The Annals of Statistics* 35, 2769 – 2794.

Van Den Heuvel, M.P., Pol, H.E.H., 2010. Exploring the brain network: a review on resting-state fmri functional connectivity. *European neuropsychopharmacology* 20, 519–534.

Van Dijk, K.R., Hedden, T., Venkataraman, A., Evans, K.C., Lazar, S.W., Buckner, R.L., 2010. Intrinsic functional connectivity as a tool for human connectomics: theory, properties, and optimization. *Journal of neurophysiology* 103, 297–321.

Von Luxburg, U., 2007. A tutorial on spectral clustering. *Statistics and computing* 17, 395–416.

Wang, K., Li, M., Hakonarson, H., 2010. Analysing biological pathways in genome-wide association studies. *Nature Reviews Genetics* 11, 843–854.

Whitfield-Gabrieli, S., Nieto-Castanon, A., 2012. Conn: a functional connectivity toolbox for correlated and anticorrelated brain networks. *Brain connectivity* 2, 125–141.

Wilson, R.C., Zhu, E.R.H., 2008. Graph spectra for comparing graphs and trees. *Pattern Recognition* 41, 2833–2841.

Xiao, L., Stephen, J.M., Wilson, T.W., Calhoun, V.D., Wang, Y.P., 2018. Alternating diffusion map based fusion of multimodal brain connectivity networks for iq prediction. *IEEE Transactions on Biomedical Engineering* 66, 2140–2151.

Yoffe, S., Moscovich, A., Jaffe, A., 2024. Spectral extraction of unique latent variables. *arXiv preprint arXiv:2402.18741* .

Zalesky, A., Fornito, A., Bullmore, E., 2010. Network-based statistic: Identifying differences in brain networks. *NeuroImage* 53, 1197–1207.

Zhang, C., Fan, J., Yu, T., 2011. Multiple testing via fdrl for large scale imaging data. *Annals of statistics* 39, 613.

Zhao, J., Jaffe, A., Li, H., Lindenbaum, O., Sefik, E., Jackson, R., Cheng, X., Flavell, R.A., Kluger, Y., 2021. Detection of differentially abundant cell subpopulations in scRNA-seq data. *Proceedings of the National Academy of Sciences* 118, e2100293118.